Validation of a CFD-based numerical wave tank of the Wavestar WEC

C. Windt & J.V. Ringwood
Centre for Ocean Energy Research, Maynooth University, Ireland

J. Davidson
Department of Fluid Mechanics, Budapest University of Technology and Economics, Hungary

E.J. Ransley
School of Engineering, Plymouth Univeristy, UK

M. Jakobsen & M. Kramer
Department of Civil Engineering, Aalborg University, Denmark

ABSTRACT: CFD-based numerical wave tank (CNWT) models, are a useful tool for the analysis of wave energy converters (WECs). During the development of a CNWT, model validation is important, to prove the accuracy of the numerical solution. This paper presents a validation study of a CNWT model for the 1:10 scale Wavestar point-absorber device. The previous studies reported by Ransley et al. (2017) and Windt et al. (2018b) are extended in this paper, by including cases in which the power-take off (PTO) system is engaged. In this study, the PTO is represented as a simple linear damping term in the CNWT WEC model, providing a first approximation to the full PTO dynamics, to be included in the CNWT in future work. The numerical results, for surface elevation and device position, are shown to compare well with the experimental measurements.

1 INTRODUCTION

Numerical modelling of WECs using CNWTs has recently attracted increased attention (Windt et al. 2018a). The previously infeasible computational costs of CFD simulations are gradually becoming viable with modern computing resources. CNWTs have the ability to provide high-fidelity analysis of WEC performance, which can allow in-depth optimisation and performance assessment of a WEC design/concept at low TRLs and capital expenditure, as discussed by Weber (2012) and Penabla et al. (2018).

However, model validation is first required, to ensure the accuracy of the numerical results. Furthermore, the validation should consider cases where the PTO and control systems are acting on the WEC. Since, in such cases, the WEC: (1) experiences realistic operational conditions, and (2) a WEC, controlled for energy maximisation, in resonance with the incident waves, typically experiences increased nonlinear hydrodynamic behaviour (Davidson et al. 2018).

Validating a CNWT WEC model requires experimental data, typically only available from scaled model testing in a physical wave tank (PWT). A useful data set recently became available, from an experimental testing campaign performed on a 1:10 scale model of the Wavestar WEC, reported by Jakobsen et al. (2016). Ransley et al. (2017) used this data set for the validation study of a CNWT model, where numerical results of body motion and hull-pressure for a fixed and freely moving, undamped body are compared to experiments. Windt et al. (2018b) used this data set to validate different dynamic mesh motion methods in the OpenFOAM environment, against experimental free-decay tests. This data set is particularly interesting for CNWT WEC model validation, since: (1) Pressure data on the hull are recorded; (2) The 1:10 scale is larger than most PWT experiments, allowing for the monitoring of more realistic hydrodynamic and turbulence effects (Schmitt and Elsässer 2017); (3) The hydraulic PTO system operates in different conditions, i.e. undamped, damped and under reactive control. While neither Ransley et al. (2017) nor Windt et al. (2018b) considers cases in which the hydraulic PTO system is engaged, the present study aims to extend the work of these previous validation studies, by including the effect of the PTO system on the dynamic behaviour of the WEC. This acts as a stepping stone towards simulating the Wavestar device in a high-fidelity wave-to-wire numerical test-bed for WECs

that includes multi-physics simulation, with a CNWT for the hydrodynamics and high-fidelity modelling for the PTO system, as demonstrated in Penabla et al. (2018).

The remainder of the paper is organised as follows. Section 2 introduces the experimental setup and WEC characteristics from the PWT test campaign. Section 3 shows the details of the CNWT used for the numerical simulations. Section 4 describes the test cases considered in the validation study: waves-only simulations and diffraction, undamped and damped (i.e. engaged PTO) WEC test cases. Section 5 presents and discusses the results. Conclusions are drawn in Section 6 and future work is discussed in Section 7.

2 EXPERIMENTAL SETUP

The experimental data in this study, originates from PWT tests of a 1:10 scale Wavestar model (see Figure 1), conducted at the Ocean Wave Basin at Plymouth University and detailed in (Jakobsen et al. 2016).
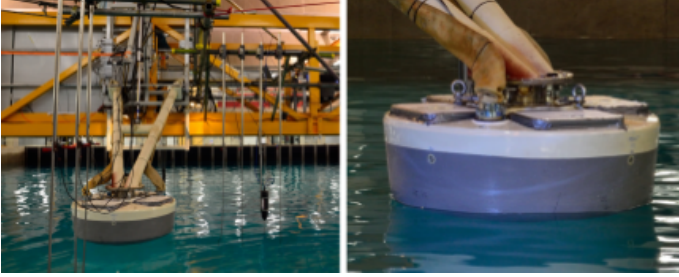

Figure 1: 1:10 scale Wavestar in Plymouth Ocean Wave basin (adapted from Ransley et al. (2017))

A schematic of the experimental test setup, including significant dimensions, is depicted in Figure 2. System properties (mass, inertia, etc.) are listed in Table 1.

In the test campaign, a number of different configurations were analysed including waves-only, fixed, undamped and damped cases. Furthermore, the device behaviour was tested in numerous monochromatic and polychromatic sea states. For the validation presented herein, the different configurations are simulated, while subject to only one of the monochromatic sea states, with wave height $H = 0.1$m and wave period $T = 1.4$s.

The body motion is experimentally measured via piston displacement of the hydraulic cylinder (see Figure 2), which will be compared to numerical results. Furthermore, free surface elevation (FSE) data, measured at various wave probes (WPs) in the PWT (see Figure 3 for WP numbering), is also used for validation. Although the WEC is also equipped with a six DoF load-cell and pressure sensors, the force and pressure data from these sensors is not considered in this validation study, due to space restrictions.

Table 1: SYSTEM PROPERTIES OF THE WAVESTAR 1:10 SCALE MODEL

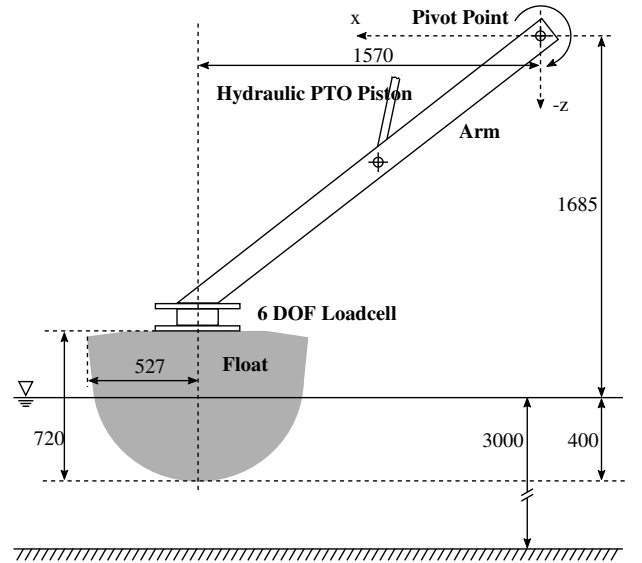|	
Mass (Float & Arm)	220kg
Inertia	124kg m^2
Centre of Mass (CoM) of the floating system in equilibrium relative to the hinge position:	
x	1.3954m
y	0.0m
z	-1.3305m
Submergence (in equilibrium)	0.4m
Water depth d	3m

Figure 2: Schematic of the experimental setup, including the main dimensions (in mm). Schematic not to scale. (Fig. adopted from Jakobsen et al. (2016), Ransley et al. (2017))
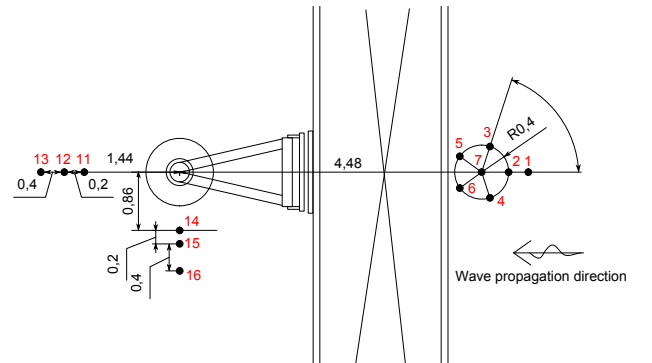

Figure 3: WP locations in the PWT; WPs numbered in red; distances in meters (adapted from Jakobsen et al. (2016))

3 NUMERICAL SETUP

This study builds upon the work by Ransley et al. (2017) and Windt et al. (2018b); thus, these studies can be consulted as useful guidelines for the numerical model setup used herein. All simulations are performed using the open-source CFD toolbox OpenFOAM (Weller et al. 1998). More specifically, the OpenFOAM Foundation fork, version 4.1 (OpenFOAM Foundation 2016), is employed.

In OpenFOAM, the Navier-Stokes equations (1)

and (2), are solved using the Finite-Volume Method (FVM). To account for the two phase flow, the Volume of Fluid (VoF) method is used.

$$\nabla \cdot \mathbf{u} = 0 \qquad (1)$$

$$\frac{\partial(\rho \mathbf{u})}{\partial t} + \nabla \cdot (\rho \mathbf{uu}) = -\nabla p + \nabla \cdot \mathbf{T} + \rho \mathbf{f}_b \qquad (2)$$

In Equations (1) and (2), t represents time, $\mathbf{u}$ the fluid velocity, p the fluid pressure, ρ the fluid density, $\mathbf{T}$ the stress tensor and $\mathbf{f}_b$ external forces such as gravity. Laminar flow conditions are assumed for all simulations, as in Ransley et al. (2017). Investigating the inclusion of turbulence modelling will be part of future work.

The body motion is solved for using OpenFOAM's *sixDoFRigidBodyMotion* solver, which calculates the body's trajectory from the forces acting upon it, via Newton's 2nd law of motion. The WEC motion is constrained to the pitch DOF in the *sixDoFRigidBodyMotion* solver. Furthermore, the PTO is included as an *angularSphericalDamper* restraint in the motion solver.

For numerical wave generation and absorption, the relaxation zone method, implemented in the *waves2Foam* toolbox (Jacobsen et al. 2012), is employed. Generally, this method requires larger domain sizes, thus longer computing times, compared to a static boundary numerical wave maker (NWM) (Windt et al. 2018). However, for the desired monochromatic sea state, preliminary studies revealed better accuracy for the *waves2Foam* wave maker, compared to the static boundary NWM *olaFOAM* (Higuera et al. 2013). No wave absorption is implemented in the y-direction.

Convergence studies, as presented in Windt et al. (2018), were performed to determine the required wave generation relaxation zone length (L_g) and wave absorption relaxation zone length (L_a). Likewise, following the convergence study outlined by Windt et al. (2018), the spatial (in the free surface and near-body region) and temporal discretisations were determined. The dimensions of the generation and absorption relaxation zone lengths, spatial and temporal discretisations, selected from the convergence studies, are listed in Table 2.

The spatial dimensions of the CNWT are 4.5m x 18.92m x 6m (WxLxH). A symmetry plane bisects the domain, to reduce the computational overhead, with the validity of exploiting symmetry in the CNWT for the Wavestar WEC being shown in Windt et al. (2018b). The total cell count of the domain is approx. 800k cells. A screen shot of the spatial discretisation in the interface and near-body region is depicted in Figure 5.
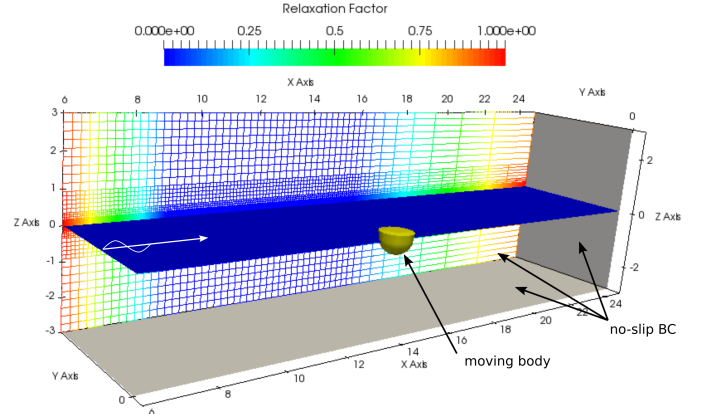

Figure 4: Numerical setup: Visualisation of the relaxation strength, free surface and the buoy hull
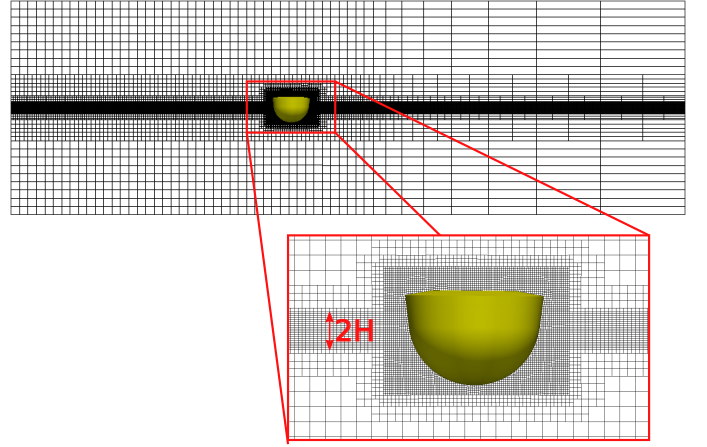

Figure 5: Spatial discretisation of the numerical domain with 10CPH and 200CPL

4 TEST CASES

The present validation study considers four different test cases, described in the following sub-sections.

4.1 *Waves-only*

A waves-only case, in which the WEC is not present in the tank, was performed in the PWT experiments to measure the incident wave field. The present validation study considers this test case first, to validate the NWM employed in the CNWT. Phase averaged free surface elevation (FSE) traces, from a zero-down crossing analysis (Windt et al. 2018), are shown for experimental and numerical results at different WP

Table 2: RELAXATION ZONE LENGTHS AND DOMAIN DISCRETISATION

Generation relaxation zone length (L_g)	1λ
Absorption relaxation zone length (L_a)	3λ
Reflection coefficient	2%
Spatial discretisation:	
dx	200CPL
dy	50CPL
dz	10CPH
Temporal discretisation	$1400^{\Delta t/T}$

locations aligned in the direction of the wave propagation (WPs 2, 7, 11 and 13).

4.2 *Diffraction*

To further validate the hydrodynamic model, and introduce wave-structure interaction (WSI), diffraction test cases are next considered for validation. In the diffraction tests, the WEC is held fixed in the PWT and CNWT and the FSE at various locations is measured. For this case, the resulting time traces, rather than the phase averaged results, are directly compared for validation purposes, to be able to show transient behaviour in the data.

4.3 *Undamped WEC*

To further validate the WSI, a test case with a freely moving body is considered. Here, in the PWT, the hydraulic fluid is drained from the PTO system, so that no additional damping, other than bearing friction or stiction, affects the body dynamics. In this case, the measured cylinder displacement in the PWT is compared to the equivalent output from the CNWT. Since, the cylinder displacement Xc is not directly measured in the CNWT, this value is calculated using geometrical transformations from the measured translational displacement of the WEC, following

$$\alpha'(t) = \alpha^* + \gamma(t) \tag{3}$$

$$Xc(t) = \sqrt{-(cos(\alpha'(t)) \cdot 2 \cdot a^* \cdot b^*) - a^{*2} - b^{*2})} \quad . \tag{4}$$

All relevant angles and distances are depicted in Figure 6, where time dependent variables are denoted with (t) and time invariant parameters with the superscript $*$. The red dot represents the reference point, tracked throughout the simulation. From the x and z displacement of the reference point, $\beta(t)$ is calculated.

4.4 *WEC with PTO damping*

Lastly, the case of a device damped through the PTO system is considered. Three different PTO settings, with linear PTO damping factors (D_{exp}) of 50, 100 and 200, are tested. In the CNWT, the PTO damping is replicated through an *angularSphericalDamper* restraint in the *sixDoFRigidBodyMotion* solver. The corresponding numerical damping values (D_{num}) are determined using data fitting with a brute force approach.
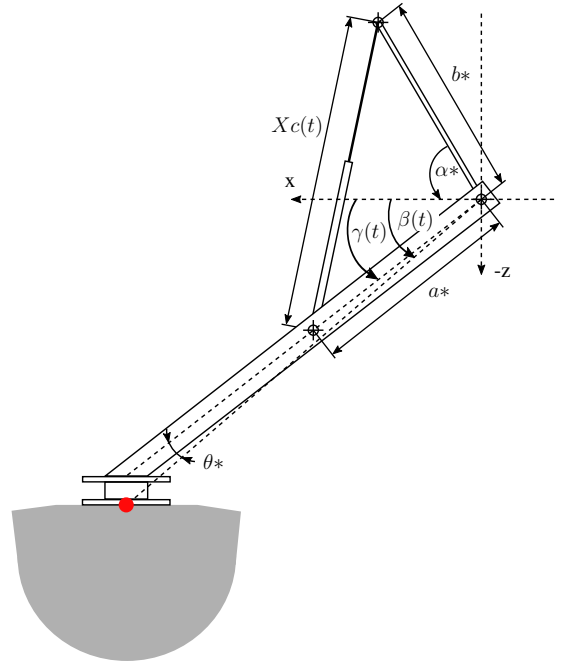

Figure 6: Relevant angles and distances for the calculation of the cylinder displacement $Xc(t)$, where time dependent variables are denoted with (t) and time invariant parameters with the superscript $*$. The red dot represents the reference point, tracked throughout the simulation. From the x and z displacement of the reference point, $\beta(t)$ is calculated.

5 RESULTS AND DISCUSSION

5.1 *Waves-only*

Figures 7 and 8 show the experimental and numerical phase averaged free surface elevation (FSE) traces, respectively. From the experimental data, considerable spatial scatter can be observed whereas, in contrast, the numerical data show consistent surface elevation measurements at the different positions.
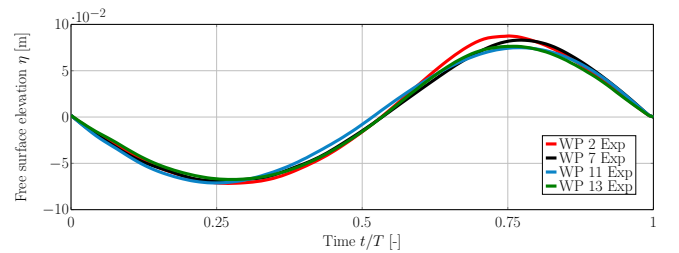

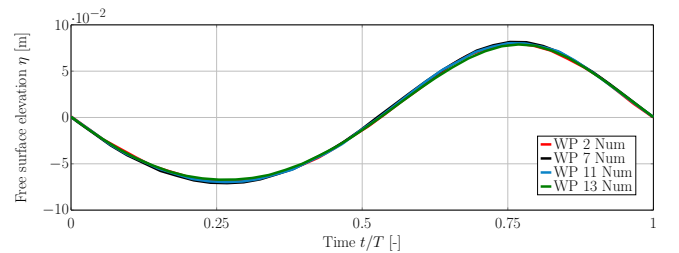Figure 7: Experimental phase averaged FSE

Figure 8: Numerical phase averaged FSE

Figure 9 shows a comparison between the experimental and numerical FSE for each WP location. Visual inspection reveals some deviations at the wave troughs at WP 7 and WP 13, showing overestimation

and underestimation, respectively, of the experimental wave trough. To quantify the deviation between experimental and numerical FSE, the root-mean-square error (RMSE) is calculated for the phase averaged FSE data following Equation 5,

$$RMSE = \sqrt{\frac{\sum_{i=1}^{N}(\eta(i)_{num} - \eta(i)_{exp})^2}{N}} \qquad (5)$$

where N is the sample length, and $\eta(i)_{num}$ and $\eta(i)_{exp}$ are the numerical and experimental FSE at each sample point i, respectively. The sample frequency is $100Hz$. Results are listed in Table 3. Overall, a good match between FSE numerical and experimental data is found.
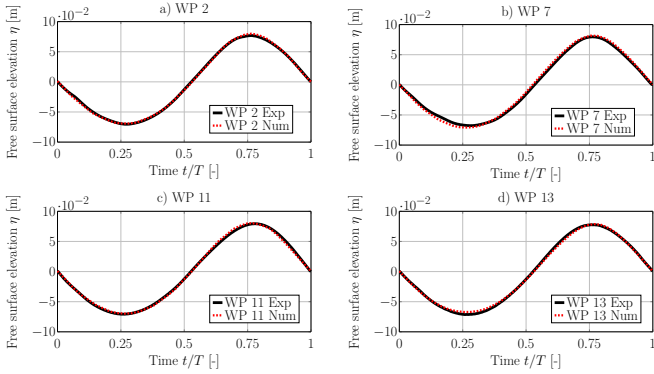

Figure 9: Comparison of numerical and experimental phase averaged FSE

Table 3: RMSE BETWEEN NUMERICAL AND EXPERIMENTAL FSE FOR WAVE-ONLY CASE

WP #	2	7	11	13
RMSE $[\cdot 10^{-3}]$	1.5	3.2	2.0	2.2

5.2 *Diffraction*

To account for the phase difference between the numerical and experimental time traces, introduced by the differences in the longitudinal extension of the tanks, the time traces are shifted relative to each other. The shift is determined based on the FSE time traces at WP 2 for the waves-only test case. The first steady state oscillation in the FSE data is used as reference point. Figure 10 shows the experimental and numerical time trace before (Figure 10 a)) and after the shift of the experimental data set (Figure 10 b)).

Using the shifted FSE time traces, the FSE for the diffraction case is evaluated at six different WP locations (see Figure 11). The quantification is again achieved by calculating the RMSE between experimental and numerical FSE data. Results are tabulated in Table 4.
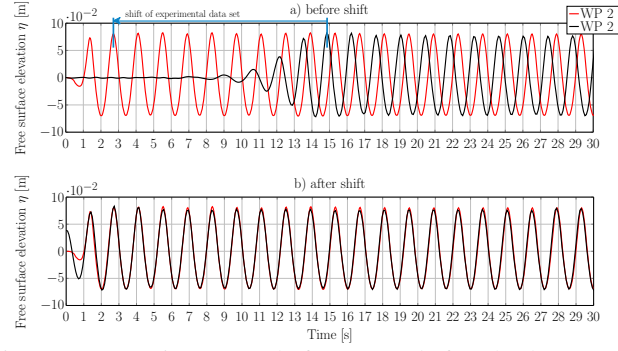The inspection of the time traces reveals a relatively close match between the two data sets for WP 2

Figure 10: FSE time traces before (a) and after (b) the correction shift, to account for different tank dimensions in the PNWT and CNWT

(RMSE $1.98 \cdot 10^{-2}$) and WP 7 (RMSE $2.25 \cdot 10^{-2}$), where at WP 7 the influence of the diffracted waves after approx. $20s$ can be seen. In the wake of the WEC, at WP 11, more significant differences can be observed (RMSE $4.09 \cdot 10^{-2}$). These deviations decay downwave and smaller deviations are found for WP 13 (RMSE $3.26 \cdot 10^{-2}$). Along the horizontal axis, at WP 14 and 16, relatively small deviations (RMSE $1.76 \cdot 10^{-2}$) are found in the vicinity of the body (WP 14), while closer to the wall, at WP 16, larger deviations (RMSE $3.10 \cdot 10^{-2}$) are measured.

In order to determine the source of the observed deviations, video footage of the experimental tank test has been inspected. It can be observed, that the physical constraints are unable to hold the WEC perfectly stationary, when subjected to the excitation force of the waves in the PWT, which, in contrast to the motionless WEC in the CNWT, may bias the diffracted wave field. Furthermore, the reflections from the PWT down- and upwave boundaries may not match the CNWT, which, again, can bias the measured wave field.
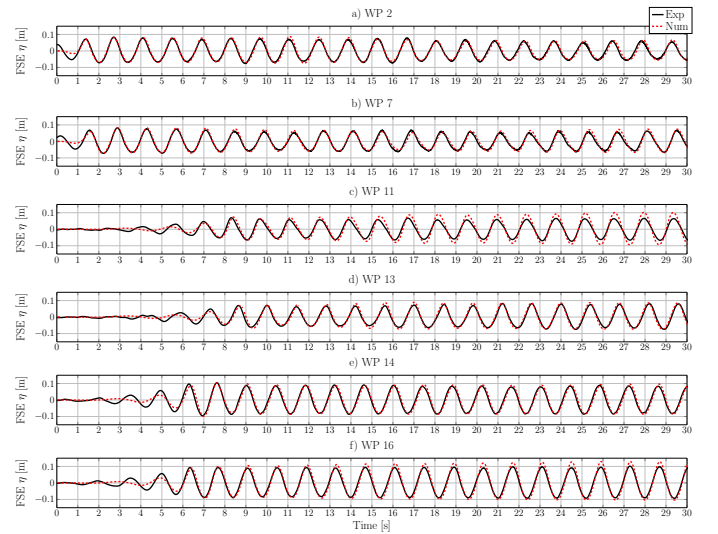

Figure 11: Experimental and numerical FSE time traces at WPs 2 (a), 7 (b), 11 (c), 13 (d), 14 (e) and 16 (f)

Table 4: RMSE BETWEEN NUMERICAL AND EXPERIMENTAL FSE FOR DIFFRACTION CASE

WP #	2	7	11	13	14	16
RMSE $[\cdot 10^{-2}]$	1.98	2.25	4.09	3.26	1.76	3.10

5.3 *Undamped WEC*

Figure 12 shows the time trace of the hydraulic cylinder displacement $Xc(t)$. For the CNWT, these have been extracted using geometrical transformations on the measured displacement of the buoy. To account for the phase difference between the physical and numerical wave signal, the experimental data are shifted, based on the results in Section 5.2. Although a match in phase is expected after applying the shift, a clear mismatch can be observed (see Figure 12 a)). Only an additional shift of $0.96s$ leads to an agreement in phase between the two cylinder displacement signals (see Figure 12 b)). It is assumed that an incorrect triggering between the wave paddle signal and the cylinder displacement signal in the PTW provokes the need for an additional shift. This assumption is underpinned by inspection of the free surface elevation at WP 16, for the undamped body case (see Figure 13). Applying the same shift, as found in the previous section, to the FSE time trace, good phase agreement is observed between experimental and numerical data.
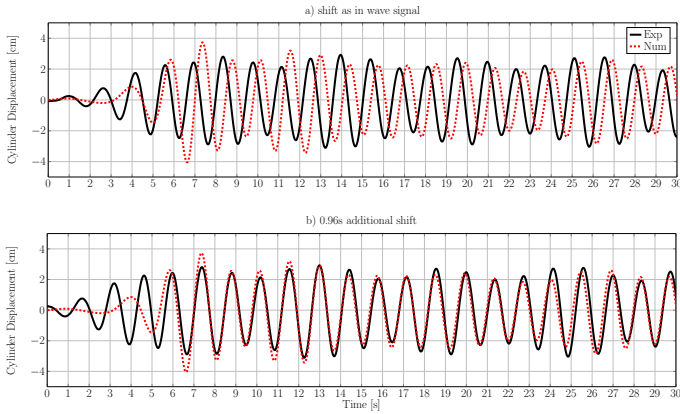

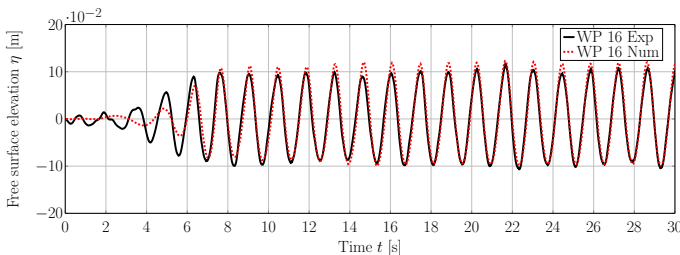Figure 12: Experimental and numerical cylinder displacement

Figure 13: Experimental and numerical FSE time traces at WP 16

Overall, large temporal scatter in the oscillation amplitude can be observed in the numerical and experimental data. It is suggested that this is the results of extensive wave reflections from the side walls of

the PWT and CNWT. Indeed, the trends of larger and smaller oscillation amplitudes are well captured by the numerical simulations up to approx. $t > 34s$. After that, it can be assumed that additional reflection from the PWT far field boundaries come into play. In fact, for the experimental analysis, Jakobsen et al. (2016) also only used the first 20 fully formed wave periods, to limit reflections from the walls and beaches. A relatively large RMSE of 0.264 is calculated between the experimental and numerical results. Interestingly, larger max./min. displacements can be observed in the experimental results, for $t > 14s$. The neglect of any additional bearing friction or suchlike in the CNWT, would however suggest larger oscillations in the numerical domain. Overall, similar results are found by Ransley et al. (2017), giving some confidence in the CNWT data. In future work, using a different monochromatic wave, the validity of these results shall be further investigated.

5.4 *WEC with PTO damping*

The cylinder displacement, surface elevation at WP 16 and the power output from the PWT for three PTO settings, i.e. 50, 100 and 200, is shown in Figure 14 a) – c). As expected, a decrease in oscillation amplitude can be observed with increasing PTO damping, while the surface elevation in line with the device is virtually unaffected by the different PTO settings. For the power output, a decrease with increasing PTO damping can be observed.
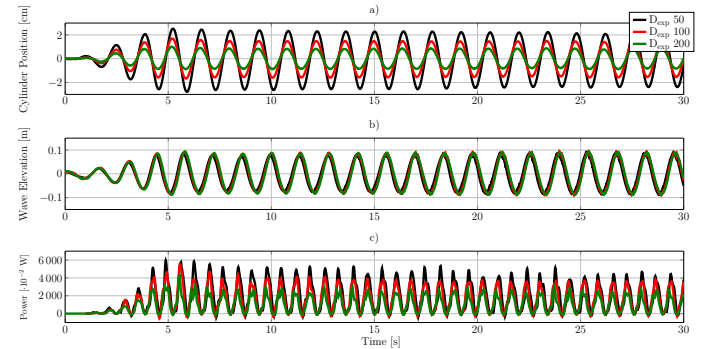

Figure 14: Experimental cylinder displacement (a)), surface elevation (at WP 16) (b)) and power output (c)) with different PTO settings

In the PWT, linear damping is applied to the PTO system. In the CNWT, rotational angular damping [Nms/rad] has been applied in this study. Thus, in a first test, using $D_{exp} = 200$, the effective rotational angular damping is determined, using a brute force approach. Results for this optimization are shown in Figure 15 and 16. Figure 15 shows a time trace snippet for the different numerical damping settings, while Figure 16 shows the relative deviation between the numerical and experimental peak and trough values, as a function of the applied angular damping.

From Figure 16, it can be seen that an excellent match for the oscillation peaks is achieved with a an-

gular damping of $3500Nms/rad$; however, a residual error of 10% can be observed for the troughs. This suggests the need for damping additional to the linear damping in the PWT. A detailed investigation of this additional damping will be part of future work.
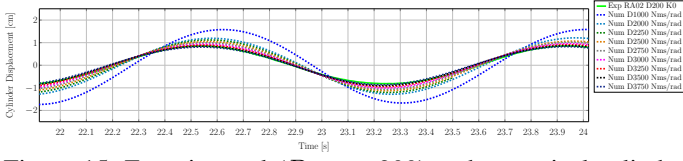

Figure 15: Experimental ($D_{exp} = 200$) and numerical cylinder displacement for different PTO settings
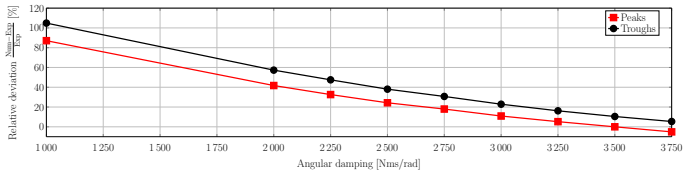

Figure 16: Relative deviation between numerical and experimental ($D_{exp} = 200$) peak and trough values of the cylinder displacement for different PTO settings

To validate the damping coefficient found in the above described brute force optimisation, damping factors of $1750Nms/rad$ and $875Nms/rad$ are applied to replicate the PWT test cases of $D_{exp} = 100$ and $D_{exp} = 50$, respectively. Time traces for all three test cases are shown in Figures 17 to 19, while the corresponding RMSE values are listed in Table 5. Additionally, the mean power output from the numerical simulations and the experimental tests are listed in Table 6.

As expected, Table 5 shows the smallest RMSE value ($3.61 \cdot 10^{-2}$m) for the case of $D_{exp} = 200$, for which the optimisation has been performed. In fact, this is approx. half the RMSE found in the undamped case. The relatively good match between experiments and numerics is also highlighted in the plot of cylinder displacement, Figure 17, where the aforementioned, larger mismatch at the oscillation troughs can be observed. Generally, compared to the undamped case, a more regular cylinder displacement can be observed when engaging the PTO. This can be attributed the reduction of wave reflection in the tank due to smaller body motions.

For decreasing damping values, Table 5 shows increasing RMSE values. Inspection of Figures 18 and 19 reveals that the predicted damping coefficient in the numerical simulations leads to an underestimation of the cylinder displacement amplitudes. It can be assumed that, in the case of the largest damping, the PTO dynamics effect the motion of the body in a different way to that for lower damping values. Since the brute force approach was used for the largest damping case, these dynamics are accounted for and thus, lead to a mismatch in the body motion for the lower damping values.

In neglected influence of PTO dynamics and mechanical damping can furthermore be observed in the mean power output (see Table 6). Although smallest RMSE in the device position (and thus velocity) is seen for the largest damping, the highest relative deviation in power is found for this case. The deviation can directly be attributed to deviations in the force signal, i.e. overestimation of the PTO force. The deviations in power output for the cases of $D_{exp} = 100$ and $D_{exp} = 50$ do follow the trend of the cylinder displacement. The case of $D_{exp} = 100$, with a RMSE of $6.7 \cdot 10^{-2}$m shows a relative deviation in power of 6.8%. The case of $D_{exp} = 50$, with a RMSE of $13.5 \cdot 10^{-2}$m shows a relative deviation in power of 19.4%. To clarify the source of the deviation, a thorough study on the modelling of the damping components affecting the body dynamics (mechanical friction and stiction, PTO losses, etc.) will be part of future work.
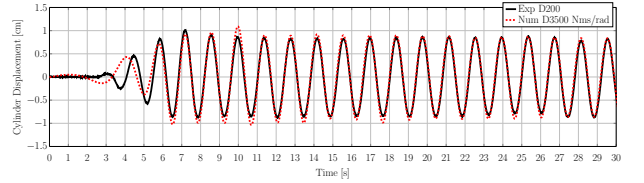

Figure 17: Numerical and experimental cylinder displacement for $D_{num} = 3500Nms/rad$ and $D_{exp} = 200$

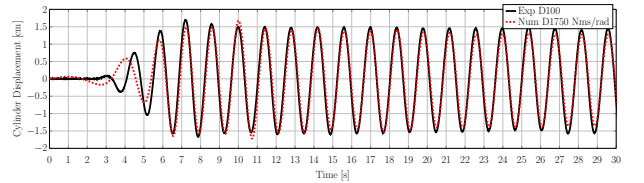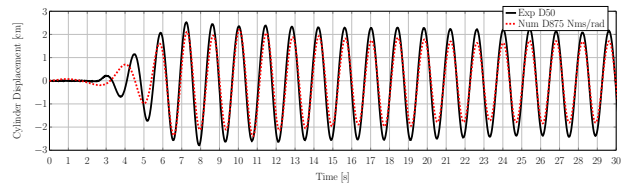Figure 18: Numerical and experimental cylinder displacement for $D_{num} = 1750Nms/rad$ and $D_{exp} = 100$

Figure 19: Numerical and experimental cylinder displacement for $D_{num} = 875Nms/rad$ and $D_{exp} = 50$

Table 5: RMSE BETWEEN NUMERICAL AND EXPERIMENTAL CYLINDER DISPLACEMENT

D_{exp}		200	100	50
D_{num}	[Nms/rad]	3500	1750	875
RMSE	[$\cdot 10^{-1}$m]	0.36	0.67	1.35

Table 6: MEAN POWER OUTPUT AND RELATIVE DEVIATION FROM NUMERICAL SIMULATIONS AND EXPERIMENTS

D_{exp}		200	100	50
D_{num}	[Nms/rad]	3500	1750	875
P_{exp}	[W]	9.9	14.6	17.15
P_{num}	[W]	12.85	15.6	13.82
$|\epsilon|$	[%]	29.8	6.8	19.4

6 CONCLUSIONS

From the results of the different validation test cases, four essential conclusions can be drawn:

- The experimental data are subject to measurement uncertainty and some unquantifiable effects, such as mechanical friction, rendering the validation a challenging task.

- The numerical setup is able to accurately generate the desired wave field and shows a relatively good match with the experimental data, especially considering the significant spatial scatter of the wave field in the PWT.

- The WSI, for the case of a fixed, diffracting, body is well captured in the CNWT and the hydrodynamic model is effectively validated.

- The WSI, for the case of a moving body, under different conditions, shows a difference in accuracy depending of the particular case. General trends of the body dynamics are captured; however, for a full validation, more in-depth studies on the representation of the mechanical system in the CNWT are needed.

7 FUTURE WORK

In a follow-up study to the present paper, the hydrodynamic model will be further validated using different monochromatic and polychromatic sea states, and will also include reactive control cases. The validated model will then be coupled to a high-fidelity PTO model (Penabla et al. 2018) in order to enable analysis of the effect of turbulence modelling, and scaling, under realistic conditions.

REFERENCES

Davidson, J., C. Windt, G. Giorgi, R. Genest, & J. Ringwood (2018). *OpenFOAM : Selected papers from the 11th Workshop*, Chapter Evaluation of energy maximising control systems for wave energy converters using OpenFOAM. Springer.

Higuera, P., J. L. Lara, & I. J. Losada (2013). Realistic wave generation and active wave absorption for NavierStokes models Application to OpenFOAM. *Coastal Engineering*.

Jacobsen, N., D. R. Fuhrmann, & J. Fredsoe (2012). A wave generation toolbox for the open-source CFD library: OpenFoam(R). *International Journal for Numerical Methods in Fluids*.

Jakobsen, M. M., S. Beatty, G. Iglesias, & M. M. Kramer (2016). Characterization of loads on a hemispherical point absorber wave energy converter. *International Journal of Marine Energy 13*, 1–15.

OpenFOAM Foundation (2016). OpenFOAM 4.1 release notes. https://openfoam.org/download/4-1-ubuntu/.

Penabla, M., J. Davidson, C. Windt, & J. Ringwood (2018). A high-fidelity wave-to-wire simulation platform for wave energy converters: Coupled numerical wave tank and power take-off models. *Submitted to Applied Energy*.

Ransley, E., D. Greaves, A. Raby, D. Simmonds, M. Jakobsen, & M. Kramer (2017, aug). RANS-VOF modelling of the wavestar point absorber. *Renewable Energy 109*, 49–65.

Schmitt, P. & B. Elsässer (2017). The application of Froude scaling to model tests of Oscillating Wave Surge Converters. *Ocean Engineering 141*, 108–115.

Weber, J. (2012). Wec technology readiness and performance matrix–finding the best research technology development trajectory. In *Int. Conf. Ocean Energy Dublin Irel*.

Weller, H. G., G. Tabor, H. Jasak, & C. Fureby (1998). A tensorial approach to computational continuum mechanics using object-oriented techniques. *Computers in Physic 12*(6), 620 – 631.

Windt, C., J. Davidson, & J. Ringwood (2018a). High-fidelity numerical modelling of ocean wave energy systems: A review of cfd-based numerical wave tanks. *submitted to Renewable and Sustainable Energy Reviews*.

Windt, C., J. Davidson, & J. Ringwood (2018b). Performance assessment of the overset grid method for numerical wave tank experiments in the OpenFOAM environment. In *Proceedings of the ASME 2018 37th International Conference on Ocean, Offshore and Arctic Engineering*.

Windt, C., J. Davidson, P. Schmitt, & J. Ringwood (2018). A benchmark study for numerical wave makers in cfd simulations. *submitted to Coastal Engineering*.